2022 44th Annual International Conference of
the IEEE Engineering in Medicine & Biology Society (EMBC)
Scottish Event Campus, Glasgow, UK, July 11-15, 2022

2022 44th Annual International Conference of the IEEE Engineering in Medicine & Biology Society (EMBC) | 978-1-7281-2782-8/22/$31.00 ©2022 IEEE | DOI: 10.1109/EMBC48229.2022.9871526

CNN-Based Classification of Craniosynostosis Using 2D Distance Maps

Matthias Schaufelberger[1], Reinald Peter Kühle[2], Christian Kaiser[1], Andreas Wachter[1], Frederic Weichel[2], Niclas Hagen[3], Friedemann Ringwald[3], Urs Eisenmann[3], Christian Freudlsperger[2], Werner Nahm[1]

***Abstract*— Craniosynostosis is a condition associated with the premature fusion of skull sutures affecting infants. 3D photogrammetric scans are a promising alternative to computed tomography scans in cases of single suture or nonsyndromic synostosis for diagnostic imaging, but oftentimes diagnosis is not automated and relies on additional cephalometric measurements and the experience of the surgeon.**

We propose an alternative representation of the infant's head shape created from 3D photogrammetric surface scans as 2D distance maps. Those 2D distance maps rely on ray casting to extract distances from a center point to the head surface, arranging them into a 2D image grid. We use the distance map for an original convolutional neural network (CNN)-based classification approach, which is evaluated on a publicly available synthetic dataset for benchmarking and also tested on clinical data.

Qualitative differences of different head shapes can be observed in the distance maps. The CNN-based classifier achieves accuracies of 100 % on the publicly available synthetic dataset and 98.86 % on the clinical test set.

Our distance map approach demonstrates the diagnostic value of 3D photogrammetry and the possibility of automatic, CNN-based diagnosis. Future steps include the improvement of the mapping method and testing the CNN on more pathologies.

***Clinical relevance*— The gold standard for the diagnosis of craniosynostosis is computed tomography imaging. Yet, this exposes infants to ionizing radiation which should be avoided due to an increased risk of developing intracranial neoplasms or leukemia. This contribution proposes a mapping method to obtain 2D images from 3D head surface scans, enabling a radiation-free, CNN-based diagnosis of craniosynostosis.**

I. INTRODUCTION

Craniosynostosis is a condition caused by the premature fusion of one or more skull sutures in infants and has an estimated prevalence of four cases per 10,000 live births [1]. Craniosynostosis is linked to elevated intracranial pressure [2] which can reduce neuropsychological development. The premature closure of a suture limits the head growth perpendicular to the suture and causes compensatory parallel growth leading to characteristic head shapes. During diagnosis, physicians perform visual examination, palpation, cephalometric measurements, and medical imaging e.g., computed tomography (CT). CT is the gold standard imaging method for craniosynostosis diagnosis, but exposes the infants to ionizing radiation. 3D photogrammetric surface scans provide an inexpensive, radiation-free, and fast diagnostic tool that might even be used for screening in general medical practice or pediatric care.

Researchers studied head deformities in terms of shape characteristics and asymmetry both on CT data [3] and surface scans [4]. Other studies determined the relationship between the two domains [5]. Multiple contributions introduced approaches to classify craniosynostosis on CT data [3] and surface scans [6], [7] and obtained accuracies between 95.7 % and 99.5 %, each on different in-house datasets.

In this contribution we introduce a method to create a 2D distance map for each scan enabling an automatic classification for common types of craniosynostosis using a CNN. We expand on ideas from a mapping approach concerned with head asymmetry [4] and combine it with ray casting which is also popular for classification [6]. Compared to competing classification methods, our approach uses a 2D image representation as an intermediate step for a CNN. Our model is the first to be tested on a publicly available synthetic dataset for benchmarking, enabling comparisons between different classifiers.

II. MATERIALS AND METHODS

The workflow for the distance map creation and classification is shown in Fig. 1. We apply ray casting to extract distances from a center point and arrange them in a two-dimensional grid, used as an input image for a CNN. We continue with a description of the three parts of the schematic.

A. Dataset

We use a synthetic dataset of craniosynostosis patients created using a statistical shape model developed in our group in a previous work [7], which is publicly available on Zenodo [8]. The dataset contains four classes of head shapes with 100 instances each. We give an overview of the head shapes in Fig. 2. Three out of four classes show different types of craniosynostosis (coronal, metopic, and sagittal synostosis) while the fourth class functions as the control class constructed from non-synostotic infants.

For the creation of the synthetic samples we refer to [7]. Regarding the clinical data, we considered the original 367 patients with the same classes from which the synthetic

This work received funding by the HEiKA research project grant HEiKA_19-17. The authors acknowledge the support by the state of Baden-Württemberg through bwHPC.

[1]Matthias Schaufelberger, Christian Kaiser, Andreas Wachter, and Werner Nahm are with the Institute of Biomedical Engineering (IBT), Karlsruhe Institute of Technology (KIT), Kaiserstr. 12, 76137 Karlsruhe, Germany publications@ibt.kit.edu

[2]Reinald Kühle, Frederic Weichel, and Christian Freudlsperger are with the Department of Oral and Maxillofacial Surgery, Heidelberg University Hospital, Im Neuenheimer Feld 400, Heidelberg, Germany

[3]Niclas Hagen, Friedemann Ringwald, and Urs Eisenmann are with the Institute of Medical Informatics, Heidelberg University Hospital, Im Neuenheimer Feld 130.3, Heidelberg, Germany

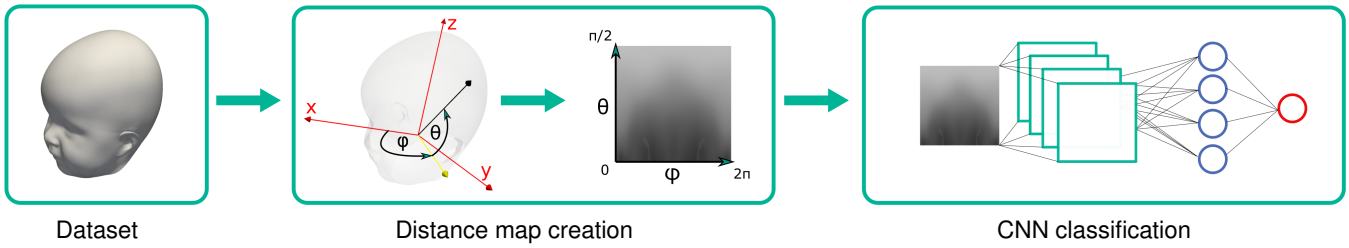

Fig. 1. Workflow of the distance map creation and subsequent classification.

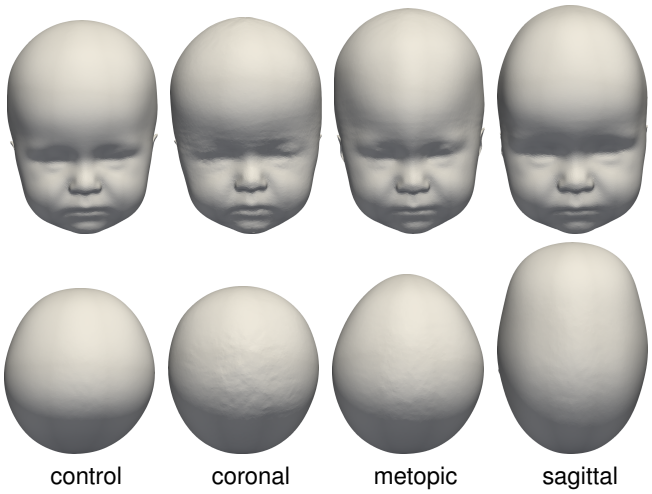

Fig. 2. Head shapes of the four classes in the dataset. Top row: front view, bottom row: top view.

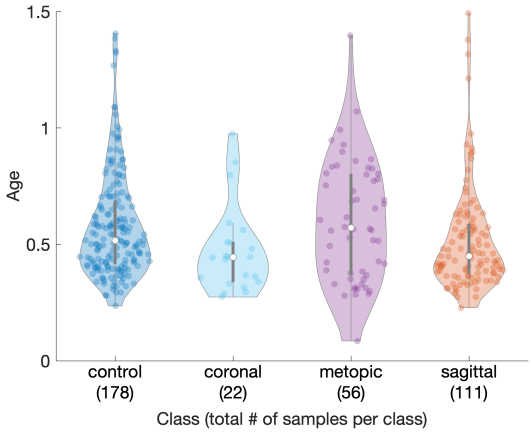

Fig. 3. Age distributions of the clinical dataset. Parentheses indicate the number of samples per class.

dataset was created. We used a standardized protocol, which had been examined and approved by the Ethics Committee Medical Faculty of the University of Heidelberg (Ethics number S-237/2009). The study was carried out according to the Declaration of Helsinki and written informed consent was obtained from parents. The age distribution and the number of subject of each class are presented in Fig. 3. All subjects diagnosed with craniosynostosis underwent surgical cranial remodeling of the skull. In contrast, the control class consists of children without head deformities and children diagnosed with non-synostotic, positional plagiocephaly.

All clinical scans had been annotated with cephalometric landmarks by clinical experts. For our contribution, we used the sellion $\mathbf{p}_\mathrm{s}$ located on the nose as well as the otobasion superius left and right ($\mathbf{p}_\mathrm{osl}$ and $\mathbf{p}_\mathrm{osr}$) located on the ears. The synthetic instances were derived from the statistical shape model [8] and are in dense correspondence, meaning that the point identifiers share the same anatomic meaning. Thus, we determined the landmark positions on the mean shape and used the same identifiers across all instances.

B. Distance Map Creation

The ray casting requires a coordinate system shared across all scans. First, we defined the center point $\mathbf{p}_\mathrm{c}$ as the midpoint between left and right otobasion superius:

$$\mathbf{p}_\mathrm{c} = \frac{1}{2}\left(\mathbf{p}_\mathrm{osl} + \mathbf{p}_\mathrm{osr}\right) \tag{1}$$

Second, we define the three axis directions $\mathbf{u}_\mathrm{x}$, $\mathbf{u}_\mathrm{y}$, and $\mathbf{u}_\mathrm{z}$, where $\mathbf{u}_\mathrm{x}$ is the direction from the center point to the sellion:

$$\mathbf{u}_\mathrm{x} = \mathbf{p}_\mathrm{s} - \mathbf{p}_\mathrm{c} \tag{2}$$

$\mathbf{u}_\mathrm{y}$ is the part from the center to the left otobasion superius orthogonal to $\mathbf{u}_\mathrm{x}$:

$$\mathbf{u}_\mathrm{y} = (\mathbf{p}_\mathrm{obl} - \mathbf{p}_\mathrm{c}) - \mathbf{u}_\mathrm{x}\frac{\mathbf{u}_\mathrm{x}\cdot(\mathbf{p}_\mathrm{obl} - \mathbf{p}_\mathrm{c})}{||\mathbf{u}_\mathrm{x}||} \tag{3}$$

$\mathbf{u}_\mathrm{z}$ is constructed to be orthogonal to the two previous directions:

$$\mathbf{u}_\mathrm{z} = \mathbf{u}_\mathrm{x} \times \mathbf{u}_\mathrm{y} \tag{4}$$

The direction vectors $[\mathbf{u}_\mathrm{x}, \mathbf{u}_\mathrm{y}, \mathbf{u}_\mathrm{z}]^\mathsf{T}$ are then normalized to obtain an orthonormal basis $[\mathbf{e}_\mathrm{x}, \mathbf{e}_\mathrm{y}, \mathbf{e}_\mathrm{z}]^\mathsf{T}$:

$$\left[\mathbf{e}_\mathrm{x}, \mathbf{e}_\mathrm{y}, \mathbf{e}_\mathrm{z}\right]^\mathsf{T} = \left[\frac{\mathbf{u}_\mathrm{x}}{||\mathbf{u}_\mathrm{x}||}, \frac{\mathbf{u}_\mathrm{y}}{||\mathbf{u}_\mathrm{y}||}, \frac{\mathbf{u}_\mathrm{z}}{||\mathbf{u}_\mathrm{z}||}\right]^\mathsf{T} \tag{5}$$

Third, we defined the ray directions similar to the horizontal coordinate system. The two angles φ and θ are comparable to azimuth and altitude and their relation to the coordinate axes are visualized in Fig. 4. The final ray directions were determined by uniformly sampling the two angles φ and θ in the intervals $0 \leq \varphi < 2\pi$ and $0 \leq \theta < \pi/2$. By using a spherical coordinate transformation, the direction $\mathbf{d}$ of each ray is given by the following equation:

$$\mathbf{d} = \left[\cos\varphi\cos\theta, \sin\varphi\cos\theta, \sin\theta\right]^\mathsf{T} \tag{6}$$

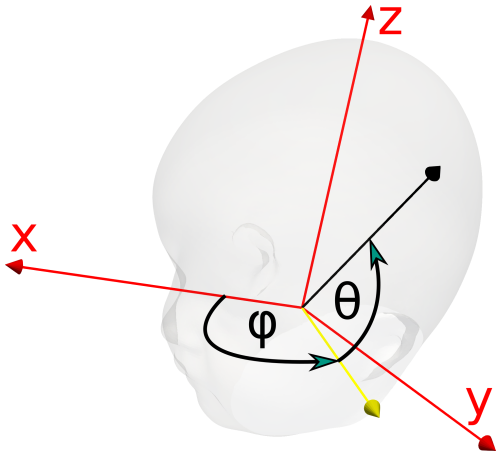

Fig. 4. Visualization of the angle definitions. Red: coordinate axes, black: cast ray, yellow: visualized ray in bottom plane, φ: azimuth, θ: altitude.

As many pre-trained CNNs use an input image size of 224×224 pixels, we divided each angle interval in 224 equidistant steps. This number is an arbitrary choice which facilitates the later use of the distance maps for CNNs. For each ray, we computed the intersection with the triangular surface mesh. For the intersected faces, we used barycentric coordinates to determine the exact hit point and computed the distance to the center points. The distances were stored in a 2D array, visualized in Fig. 5.

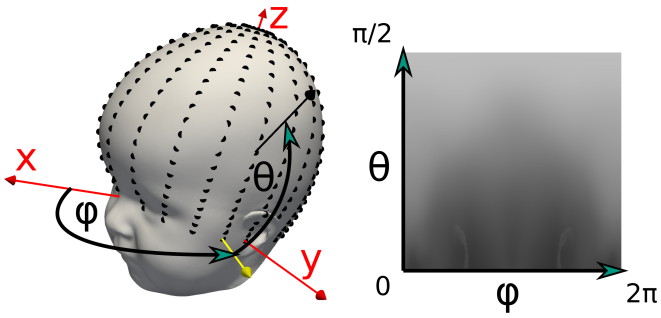

Fig. 5. Left: Visualization of 20×20 hit points with equidistant φ and θ. Right: 224×224 ray distances arranged in a 2D distance map.

Before converting the ray distances to an image they were normalized. We computed mean μ and standard deviation σ across all distances in each dataset. All distances were linearly transformed from the interval $[\mu - 3\sigma, \mu + 3\sigma]$ to the standard grayscale image intensity range $[0, 255]$. This rescaling in the image domain can be geometrically interpreted as an isotropic rescaling of all scans by the same scaling factor, leaving geometric relations between parts of the head intact.

C. CNN Classification

We chose a pre-trained *ResNet18* model over other models such as *VGG11* or *GoogleNet* as it is a very popular model which has comparatively few trainable parameters. We replaced the final layer to match the number of classes and performed two experiments: first on synthetic data and second on clinical data. Both CNNs were trained using the same hyperparameters which we present in Table I.

- Synthetic dataset:
  The training setup for the first CNN using the publicly available synthetic dataset [8] enables benchmarking across different groups. We used stratified 10-fold cross-validation.
- Clinical dataset:
  The second CNN was trained on the clinical dataset, also using a stratified 10-fold cross-validation for training and test data, so the same train-test class imbalance was shared among folds. To prevent cross-over, no synthetic data was used.

TABLE I
CNN HYPERPARAMETERS FOR SYNTHETIC AND CLINICAL DATA.

Training approach	Fine-tuning of pre-trained *ResNet18*
Optimizer	Adam
Learning rate	$\alpha = 10^{-3}$
Weight decay	$\gamma = 10^{-1}$ each 10 steps
Number of epochs	$n = 100$

III. RESULTS

A. Distance maps

We compare the resulting distance maps qualitatively. As an example, we present the distance maps for the mean shapes in Fig. 6 as the most representative cases. Differences between the classes are mildly visible. The sagittal and the metopic mean shape show two dark areas on the left and right side of the image, separated by a brighter area in the middle. In contrast, the control and coronal model show one larger, dark region. The two ears are clearly visible for all four cases as brighter curved shapes at the bottom of the image. All images have a top-to-bottom color gradient from bright to dark gray.

B. Classification

For the synthetic data, the accuracy of training and test set was 100 %. Regarding the clinical data, the final classification result on the test set was 98.4 %. We show the full confusion matrix including per-class sensitivities and per-class specificities in Table II.

TABLE II
CONFUSION MATRIX FOR THE CLINICAL DATASET.

True class	Predicted class				Sensitivity	Specificity
	Control	Coronal	Metopic	Sagittal		
Control	177	1	0	0	0.994	0.979
Coronal	2	20	0	0	0.909	0.997
Metopic	0	0	55	1	0.982	1.000
Sagittal	2	0	0	109	0.982	0.996
Total accuracy						0.984

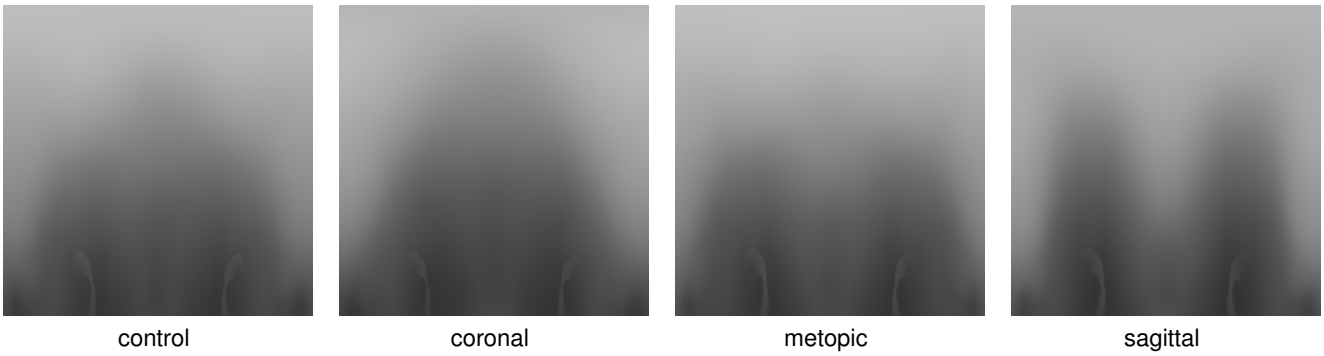

Fig. 6. Distance maps of the mean shapes of each class. For the image axes, we refer to Fig. 5. A brighter color indicates a larger distance from the center point. Intensity translated to real-world distances $d = 25.80\,\text{mm} + n_{\text{pixel}} \cdot 0.53\,\text{mm}$.

IV. DISCUSSION

The 2D distance maps show mild differences between the different pathological classes, implying that they enable a quantification of head shape. As such they are currently difficult to interpret and might be extended by other metrics such as asymmetry [4] or curvature. Additionally, the color gradient in the resulting images indicates that the distances for rays with $\theta \approx \pi/2$ lead to larger distances than rays with $\theta \approx 0$. As a consequence, the intensity range is not used to its full capacity yet. By moving the center point closer to the tip of the head (in positive direction of the y-axis), the extracted distances would have a smaller range, making better use of the 255 intensity values.

Our approach uses isotropic scaling for a equal rescaling of all head geometries. This requires a large intensity range leading to poor contrast in a single image. To improve detail, each distance map could be rescaled individually to $[0, 255]$. This has the disadvantage of disregarding the encoded information about the real-world size of the head and assumes that size is not a relevant classification parameter.

While using the two independent angles φ and θ as the two image coordinates enables the image to be easily used as an input for CNNs, this approach comes with the disadvantage that the hit points on the tip of the head are close to each other. For $\theta = \pi/2$, the same hit point is sampled multiple times regardless of φ. However, our main motivation to choose this approach was that the spatial relationship of the geometry is retained. The filter kernels of the CNN effectively take neighboring regions of the head into account. Retaining the spatial relationship is generally considered one of the main advantages of CNNs. However, dense neural networks also proofed to be capable of distinguishing head shapes [6], despite ignoring the spatial relationships of the rays.

Regarding the classification, the datasets were relatively small and no data augmentation was performed. Both a larger dataset and data augmentation would very likely be beneficial to the robustness of the classifier. A comparison of different CNNs using the same the distance maps should be considered as well as a comparisons with competing classification methods on the same dataset.

One limitation of our current approach is the highly non-interpretable usage of the *ResNet18*. Image-based or morphology-based classifiers should be tested alternatively.

V. CONCLUSIONS

We introduced a method to create distance maps enabling a visualization of the head shapes in a 2D image. We showed that a CNN was capable of classifying different head shapes on both synthetic and clinical data. This demonstrates that 3D photogrammetric scans have diagnostic value and might aid physicians to assess and diagnose head deformities such as craniosynostosis. Future work will focus on improving the algorithm, adding more pathologies, and comparing the approach to competing methods.

REFERENCES

[1] S. L. Boulet, S. A. Rasmussen, and M. A. Honein, "A population-based study of craniosynostosis in metropolitan Atlanta, 1989–2003," *American Journal of Medical Genetics Part A*, vol. 146A, no. 8, pp. 984–991, Apr. 2008.

[2] D. Renier, C. Sainte-Rose, D. Marchac, and J.-F. Hirsch, "Intracranial pressure in craniostenosis," *Journal of Neurosurgery*, vol. 57, no. 3, pp. 370–377, Sep. 1982.

[3] C. S. Mendoza, N. Safdar, K. Okada, E. Myers, G. F. Rogers, and M. G. Linguraru, "Personalized assessment of craniosynostosis via statistical shape modeling," *Medical Image Analysis*, vol. 18, no. 4, pp. 635–646, May 2014.

[4] S. Lanche, T. A. Darvann, H. Ólafsdóttir, N. V. Hermann, A. E. Van Pelt, D. Govier, M. J. Tenenbaum, S. Naidoo, P. Larsen, S. Kreiborg, R. Larsen, and A. A. Kane, "A Statistical Model of Head Asymmetry in Infants with Deformational Plagiocephaly," in *Image Analysis*, 2007, vol. 4522, pp. 898–907.

[5] A. Borghi, N. Rodriguez Florez, F. Ruggiero, G. James, J. O'Hara, J. Ong, O. Jeelani, D. Dunaway, and S. Schievano, "A population-specific material model for sagittal craniosynostosis to predict surgical shape outcomes," *Biomechanics and Modeling in Mechanobiology*, vol. 19, no. 4, pp. 1319–1329, Aug. 2020.

[6] G. de Jong, E. Bijlsma, J. Meulstee, M. Wennen, E. van Lindert, T. Maal, R. Aquarius, and H. Delye, "Combining deep learning with 3D stereophotogrammetry for craniosynostosis diagnosis," *Scientific Reports*, vol. 10, no. 1, p. 15346, Dec. 2020.

[7] M. Schaufelberger, R. P. Kühle, A. Wachter, F. Weichel, N. Hagen, F. Ringwald, U. Eisenmann, J. Hoffmann, M. Engel, C. Freudlsperger, and W. Nahm, "A statistical shape model for radiation-free assessment and classification of craniosynostosis," *arXiv:2201.03288 [cs, eess]*, Jan. 2022.

[8] M. Schaufelberger, R. P. Kühle, A. Wachter, F. Weichel, N. Hagen, F. Ringwald, U. Eisenmann, J. Hoffmann, M. Engel, C. Freudlsperger, and W. Nahm, "A statistical shape model of craniosynostosis patients and 100 model instances of each pathology," Nov. 2021. [Online]. Available: https://doi.org/10.5281/zenodo.5638148